Article:
Kepaptsoglou, D, Hardcastle, TP, Seabourne, CR et al. (8 more authors) (2015) Electronic Structure Modification of Ion Implanted Graphene: The Spectroscopic Signatures of p- and n-Type Doping. ACS Nano, 9 (11). pp. 11398-11407. ISSN 1936-0851

https://doi.org/10.1021/acsnano.5b05305

Electronic Structure Modification of Ion Implanted Graphene: the Spectroscopic Signatures of p- and n-type Doping

Demie Kepaptsoglou[1*], Trevor P. Hardcastle[2], Che R. Seabourne[2], Ursel Bangert[3,4], Recep Zan[3,5], Julian Alexander Amani[6], Hans Hofsäss[6], Rebecca J. Nicholls[7], Rik Brydson[2], Andrew J. Scott[2] and Quentin M. Ramasse[1*]

[1]*SuperSTEM Laboratory, SciTech Daresbury Campus, Daresbury WA4 4AD, United Kingdom*

[2]*Institute for Materials Research, SCaPE, University of Leeds, Leeds LS2 9JT, United Kingdom*

[3]*School of Materials, University of Manchester, Manchester, M13 9PL, United Kingdom*

[4]*current address: Department of Physics and Energy, University of Limerick, Limerick, Ireland*

[5]*current address: Department of Physics, Faculty of Arts and Sciences, Niğde University, Niğde 51000, Turkey*

[6]*II. Physikalisches Institut, Georg-August-Universität Göttingen, Friedrich-Hund-Platz 1, 37077 Göttingen, Germany*

[7]*Deparment of Materials, University of Oxford, Parks Road, Oxford OX1 3PH, United Kingdom*

Address correspondence to

*dmkepap@superstem.org, *qmramasse@superstem.org

Abstract

A combination of scanning transmission electron microscopy, electron energy loss spectroscopy, and *ab initio* calculations is used to describe the electronic structure modifications incurred by free-standing graphene through two types of single-atom doping. The N *K* and C *K* electron energy loss transitions show the presence of π^* bonding states, which are highly localised around the N dopant. In contrast the B *K* transition of a single B

dopant atom shows an unusual broad asymmetric peak which is the result of delocalised π* states away from the B dopant. The asymmetry of the B *K* towards higher energies is attributed to highly-localised σ* anti-bonding states. These experimental observations are then interpreted as direct fingerprints of the expected p- and n-type behaviour of graphene doped in this fashion, through careful comparison with density functional theory calculations.

Keywords: *graphene, doping, electronic structure, STEM, EELS, ab-initio calculations, DFT*

Graphene, a material comprised of a single layer of carbon atoms arranged in a honeycomb lattice, has in the last few years generated a true research frenzy[1,2] including production methods,[3,4] physical properties[5–7] and novel applications.[8,9] The attraction lies in graphene's outstanding electronic properties, in particular its high carrier mobility,[10] which if harnessed efficiently have the potential to revolutionise nano-electronics. However, the application of graphene in logic-circuit-based devices such as transistors is so far limited because pure graphene is an excellent conductor or a zero-band-gap semiconductor, which effectively means such devices cannot be switched off.[11,12] Several approaches have been proposed to open a band gap in graphene, including the restriction of its physical dimensions into ribbons[13–15] and the introduction of defects or dopants.[15,16]More specifically the introduction of nitrogen or boron atoms in the graphene lattice is predicted to have a drastic effect on graphene's band structure and to lead to the opening of a band gap, thus resulting in n-type[17,18] or p-type doping,[19,20] respectively, with carrier concentrations allowing practical transistor applications. All the predictions on the exact effect of the incorporated dopant atoms in graphene suggest that the resulting band structure depends on the density and periodicity (or not) of the dopant atoms in the graphene lattice,[18,20–22] as well as on the presence of adjacent defects.[23–26] To add to the complexity of the situation, the synthesis conditions of doped graphene, which most commonly follow the chemical route, yield graphene samples of varying quality,[17] often with several types of dopant atom and defect configurations within the same specimen.[25–27] In a bid to produce uniformly-doped single-layer graphene specimens, the successful implementation of low-energy ion implantation with either N or B was recently demonstrated,[28–30] achieving retention levels of the order of ~1% in good agreement with theoretical predictions.[31] This ion-implantation technique, commonly used by the modern semiconductor industry for doping Si wafers, for instance, has the advantage of allowing the uniform incorporation over a large area of single dopants on a

pre-screened, single-layer, suspended graphene sample, and of producing comparatively few defects or ad-atom configurations.[29]

Recent progress in the application of Scanning Transmission Electron Microscopy (STEM) based spectroscopy to the study of 2-dimensional materials has demonstrated the technique's ability to fingerprint single dopant atoms in graphene[32–35] and to differentiate between different electronic structure configurations, such as trivalent and tetravalent single atom Si impurities using subtle changes in the near edge fine structure of the Si $L_{2,3}$ ionisation edge in electron energy loss spectroscopy (EELS).[33,35] In this type of study *ab initio* calculations are essential tools in rationalising the experimental observations and in providing further insight into the nature of bonding around the foreign species; such a combined STEM-EELS and *ab initio* calculations approach was also used recently to probe the bonding of single nitrogen atoms in graphene[36,37] and N-doped single-walled carbon nanotubes.[38]

Building on these early studies, this paper aims to compare the electronic structure modifications generated by both single N and B substitutional dopants in single-layer graphene samples. The fully atomically-resolved EELS experimental data not only reveals the unique bonding signature of the dopants themselves but also their impact on the lattice surrounding them, with clear modifications observed in the first and second neighbour C atoms. *Ab initio* calculations are in excellent agreement with the experiment and thus not only confirm the nature of the excited states being probed by the EELS experiments but also the electronic structure reconfiguration of the doped material around the N or B dopants, in a direct verification of the distinct p- or n-type behaviour of the doped graphene.

Results and discussion

Figures 1a and 2a show HAADF images of N- and B-implanted graphene samples, respectively. For reading clarity and to remove the effects of probe tails the images have been filtered using the double-Gaussian approach described by Krivanek *et al.*[39] (see also raw images in Figure S1 in Supplementary information provided). As described in previous work,[29] the implanted graphene samples were largely defect-free with dopant atoms found mainly in substitutional positions. Contrary to previous reports on a possible preferential substitution of dopant N atoms in the same "sub-lattice"[40] no such effect was observed in the present case, for either the N-, or B-implanted graphene samples.

The implanted single dopant atoms were stable enough under the electron beam to allow for (often multiple consecutive) 2-dimensional spectrum images to be acquired, whereby the electron probe is moved serially across a defined field of view (dashed rectangle in Figure 1a), with the EELS signal recorded at each position. The chosen experimental parameters provided enough EELS signal to be collected for unambiguous chemical fingerprinting of the single atom dopants spatially resolved within a C matrix, clearly identifying them as N and B atoms, respectively (see Figures 1c and 2c and Ref. [29]). It was also possible to observe the near-edge fine structure with an excellent signal-to-noise ratio. An in-depth analysis of this fine structure is the focus of the present work.

The N *K* edge from a single N atom recorded during one such 2D EELS map acquisition (corresponding to Figure 1a-c), is shown in Figure 1d; it consists of two sharp peaks at 401 eV and 408 eV, clearly resolvable above the noise level. These are generally attributed to electronic transitions from 1s states to empty π* and σ* anti-bonding states, respectively (and are therefore often denoted π* and σ* peaks). Their clear presence indicates an sp^2-like

character in the C–N bonding[41,42] and is in good agreement with XAS experiments of doped graphene[23]. Interestingly, the shape of the N *K* edge shown here is different to that recently reported by Warner *et al.*[43] for the same system, or to the spectra reported by Arenal *et al.*[38] for single N dopant atoms in single wall carbon nanotubes (SWCNTs); in both cases no prominent π* peak was observed. While the discrepancy with N *K* edges observed in SWCNTs could be attributed to curvature[44] and geometry effects[45] (it should be noted that in the modelling studies in this work, non-planar dopant geometries were rejected as less thermodynamically favourable structures), it is more difficult to pinpoint the exact reason for the discrepancy with the N-doped graphene system. An obvious difference may lie in the fact that Warner *et al.*[33] carried out their observations at elevated temperature. Nevertheless, here, the experiments were repeated multiple times, on several distinct N atoms, systematically yielding a clearly-discernible π* peak. The repeated fast-scanning approach devised by Ramasse *et al.*[24] to obtain high-signal-to-noise spectra from single atoms was also used and yielded again similar results. It should be noted that the experimental possibility of pyridinic defect N configurations was also considered (including theoretical calculations discussed in more detail in Hardcastle *et al.*, *in preparation*), such as those discussed by Arenal *et al.,*[38] or defects created by damage or atomic jumps.[46,47] Both possibilities can be ruled out, as the HAADF signal acquired simultaneously with the spectra (an example of which is shown in Figure 2d) unambiguously shows the N dopant in a trivalent, graphitic configuration. Moreover, although the temporal resolution of the spectrum imaging experiments would not necessarily record an atomic jump, the probability of such an event in the experimental conditions is rather low.[46,47] The differences with the present results could therefore simply be due to noise levels in previous reports, along perhaps with unintentional processing artefacts. Warner *et al.*[43] indeed mention averaging their spectral data over several acquisitions and treating them with Principle Component analysis – see Methods section

within Ref. [43] (similarly, N *K* spectra presented in Ref. [38] are smoothed using a second order polynomial filter). While this can be an effective way to increase the signal-to-noise-ratio of the acquired spectra, it may result in smearing out some of the features that lie close to the noise level.

The C *K* edges of the first (C1), second (C2) and third (C3) C neighbours of the N (N1) dopant (labelled in Figure 1b) are plotted against that of a 'pristine' graphene C atom (C4) further away in the lattice. For reading clarity the spectra have been normalised to the σ*peak (the unprocessed data are presented in Figure S2 of the supplementary material provided). The C *K* ionisation edge in graphite-related materials also typically comprises two marked peaks corresponding to transitions from 1s states to empty π* and σ* levels. The π* peak in the C *K* edge of C1 (centred at 285.7 eV) is shifted up by 0.8 eV, compared to that of the 'pristine' C4 atom (centred at 284.9 eV), in good agreement with previous observations[43]. Similarly, in accordance with Refs [36,38,43] some additional intensity is observed as a shoulder on the lower energy side of the σ* peak, between 290-292 eV. Moving from the first to the second and third neighbours, C2 and C3, respectively, the π* peak gradually shifts to lower energies, while the shoulder intensity before the σ* peak is gradually lost and the σ* peak becomes sharper.

For the first time, a similar set of experiments was carried out on a B-implanted sample, allowing a direct comparison between the electronic structure modifications resulting from the different doping processes. The B *K* edge of a single substitutional B dopant recorded during a 2D EELS map acquisition is shown in Figure 2d (see also the corresponding B map in Figure 2c). The main feature of this B *K* edge profile is a strongly asymmetric intensity 'envelope' beginning at 196 eV, with peaks at 202 eV, 206 eV and a maximum at 212 eV. Unlike the B *K* edges recorded from B doped graphene grown epitaxially on B_4C,[48] bulk

B_4C,[49] or single-layer boron nitride samples,[45,49–51] only a suppressed feature is discernible at 189 eV where one might normally expect a π* peak, complemented on the low-energy side by a weak shoulder at 188 eV. To confirm this highly unusual profile, additional high signal-to-noise-ratio B *K* spectra were acquired, by accumulating the EELS signal while using a small subscan window around the substitutional B atom, similar to the method used by Ramasse *et al.*[33] The corresponding spectra are again entirely similar to those recorded *via* spectrum imaging: see Figure S3 in the supplementary material. The spatially-resolved C *K* edges corresponding to the first (C1), second (C2) and third (C3) C neighbours of the B (B1) dopant (labelled in Figure 2b) are plotted against that of a 'pristine' graphene C atom (C4) further away in the lattice (Figure 2e). Despite the noise level it is possible to discern a broadening and loss of definition of the π* and σ* peak shapes of the C1 neighbour compared to the 'pristine' C4 atom. The definition of the C *K* π* and σ* peaks is recovered when moving towards the second (C2) and third (C3) C neighbours (Figure 2e).

The experimental results therefore point to N and B doping generating very different bonding configurations to the expected C–N and C–B atomic bonds in bulk materials and, importantly, resulting in a very different impact on the local carbon environment, which could be the clear signature of the expected n- and p-type behaviour predicted for these doped materials and which is still a subject of debate.

Ab initio calculations were therefore performed in order to understand the experimental findings and reveal the bonding between single dopant atoms and graphene. Figures 3 and 4 show the supercells of single N (Figure 3a inset) and single B (Figure 4a inset) dopant atoms in the graphene lattice, respectively; the atomic positions were fully relaxed using density functional theory (DFT) calculations prior to the supercells being used as input for ground state EELS calculations. The resulting N *K*, B *K* and C *K* theoretical spectra are plotted

against the corresponding experimental spectra (shown after subtraction of the decaying background using a power-law model) in Figures 3 and 4. The theoretical spectra were rigidly translated along the energy axis to fit the experimental spectra for reading clarity, but no stretching of the energy axis was applied. The sharp and pronounced π* and σ* peaks experimentally observed in the N *K* edge (Figure 3a) are faithfully reproduced in the calculation, supporting the argument that the N *K* spectrum presented in Ref [43] was perhaps affected by data treatment or the high temperature conditions of the experiments described therein. The simulated B *K* edge (Figure 4a) also shows a strong agreement with the experiment; both the suppressed π*-like feature as well as the broad asymmetric intensity envelope with intermediate peaks are faithfully reproduced (Figure 4a). These simulations are also in excellent agreement with previous calculations of substitutional B *K* edge spectra in graphite[49]. Similarly, the simulated C *K* edges in both systems are in good agreement with the experiments, reproducing the trends observed for the C1, C2 and C3 neighbours respectively (Figures 3 and 4). In the case of N-doped graphene (Figure 3b), the calculations agree with the experimentally-observed upshift of the π* peak of the C1 neighbour as well as the 'shoulder' observed in the σ* peak, in agreement with previous observations.[37] The calculations also reproduce the smearing of the σ* peak close to the C1 neighbour in B doped graphene as well as the broadening of the π* peak. Some minor disagreement with the simulations can nevertheless be observed, and it is anticipated that considering a higher level of theory incoporating excitonic effects (such as Bethe-Salpeter approach[52]) may help providing an even closer match.

To shed light on the nature of the states to which the core 1*s* states are being promoted during the EELS experiments, the angular-momentum-resolved density of states (DOS) was calculated for no fewer than 2688 unoccupied bands above the Fermi energy for the two

types of substitutional dopant. An important consequence of the small aperture opening angle used in the experiments is that the dipole selection rule $\Delta l = \pm 1$ can be assumed to apply to a very good approximation, meaning that the experimentally-obtained EEL spectrum primarily probes states of *p*-like character. This also means that the dipole approximation used in the theoretical EELS calculations is appropriate. Thus, the *p-like* DOS is of central importance as it is effectively the sole contributor to the theoretical and experimental EEL spectra.

For each dopant, the theoretical DOS and EELS curves were extracted from the fully-optimised ground state electronic structures using the OptaDOS package,[53,54] with the Fermi energy located at zero. No core holes were included in the calculations, so the theoretical EEL spectra result from transition probabilities associated with the occupied and unoccupied states all found from ground state DFT calculations. In order to confirm that the calculations are producing physically-reasonable results, the electronic band structures were also plotted, and it was checked that the ground state electron densities showed the expected characteristics of covalent bonding (Figure S4 of the Supplementary Information provided). It was then confirmed that the ground state densities can each be partitioned into two main components; the low-energy states whose density lies primarily in-plane between the nuclei and whose appearance is consistent with σ bonds of sp^2 character, and the higher-energy states lying just below the Fermi energy, consistent with π bonds of p_z (out-of-plane) character, as expected (Figure 5c*(i)-(ii)*). The band structures for the 4x4 supercells in both cases show a very small energy gap at the Dirac point (K_{4x4}) between the π and π* bands in excellent agreement with the rules identified by Casolo *et al.*[21] for substitutional N and B dopants. Furthermore, the Fermi energy shows a shift up into the π* band (N dopant in Figure S4a) and down into the π band (B dopant in Figure S4b), revealing the presence of a negative charge carrier (n-type) in the N supercell and of a hole charge carrier (p-type) in the B

supercell. The ground state density slices suggest that the negative charge carrier can be identified as the excess density localised on the N nucleus (Figure 5c*(i)*), and the hole, similarly, as the deficit of density localised on the B nucleus (Figure 6c*(i)*). It should be noted that an excited-state formalism beyond DFT would be necessary to model the *migration* of these charge carriers to neighbouring nuclei, because such configurations involve electron densities other than the ground state.

The insight gained from these theoretical calculations, their consistency with earlier reports in the literature which predict the creation of charge carriers under these doping conditions, and the excellent agreement with experimental data of the simulated spectra derived from them, can now be used to demonstrate how the experimental EEL spectra in this work are the spectroscopic signatures of p-type (B) and n-type (N) doping in graphene. To be a dopant, an impurity must provide a mobile charge carrier and leave the material neutral. An n-type dopant provides a negative charge carrier which is balanced by the extra proton in the dopant nucleus compared to its neighbours. Conversely, a p-type dopant provides a hole charge carrier which is balanced by the deficit of a proton compared to its neighbours.

In order to reveal the physical picture behind the EELS spectra, the plots of Figures 5a,b and 6a,b (for the N and B case, respectively) are used to select energy windows of interest, in order to attribute particular features on the spectra to particular sets of high-energy states. For each set of states that lie entirely within the energy window of interest, the corresponding electron density was constructed and plotted in Figures 5c*(iii)–(v)* and 6b*(ii)–(vi)*, respectively. Figures 5c*(ii)–(v)* show the electron density in the N supercell lying in progressively higher energy windows above the Fermi energy. The density in Figure 5c*(iii)* in the energy range 0–1.2 eV has an appearance consistent with p_z orbitals, in which the charge accumulates in opposing out-of-plane lobes about each nucleus. This suggests an

interpretation of this density as corresponding to π* anti-bonding states, and it is clear that these states are highly localised around the N nucleus and its nearest neighbours in preference to the C nuclei further away in the lattice. Thus the first theoretical N EELS peak can be readily labelled as the π* peak – as is customary. The density in the next energy window, Figure 5c*(iv)*, has an appearance consistent with that of sp^2 orbitals, or σ bonds, subjected to 60° rotations about the nuclei. Once again, the states are highly localised on the dopant. This resemblance to rotated sp^2 orbitals can be interpreted as core excitations to anti-bonding σ states, or σ* bonds, and for this reason the second intense peak in the N EEL spectrum is named as the σ* peak. In contrast to these two cases, the charge density in the much broader and higher-energy range (9.5–23.5 eV) in Figure 5c*(v)* is highly localised on the neighbouring C nuclei, and not on the N nucleus. The N nucleus has one extra positive charge compared to its C neighbours, and so it is more electronegative. It is therefore easy to rationalise the overall trend observed through Figures 5c*(iii)–(v)*: in summary, for the case of N, the energy states probed during an EELS scattering event correspond to the characteristic π* and σ* peaks which are relatively low in energy due to the greater attraction to the N nucleus, which is more electronegative than its neighbours; the direct consequence of N being an n-type donor.

Figures 6c*(ii)–(vi)* show the electron densities for the case of B doping, also in order of increasing energy. The density in Figure 6c*(ii)* coinciding with the small B *K* edge EELS peak immediately above the Fermi energy shows the p-type hole being populated with a single p_z-like state: the hole is thus localised in the p_z orbitals. Indeed, the band structure in Figure S4b of the Supplementary information provided confirms that this empty state lies in the π band, and so this first small peak is labelled as the π peak, the signature of the p-type charge carrier. This signal is observed experimentally as the weak but consistently-recorded

shoulder at 189 eV in all datasets. It should be noted that an equivalent signal is, of course, absent in for the N-doped case because there the negative charge carrier constitutes an occupied state. Following a similar style of analysis to that of the states in the N supercell, it can be seen in Figure 6c*(iii)* that p_z-like states are clearly identifiable, constituting π* anti-bonding states. Figure 6c*(iv)* shows rotated sp^2-like states, constituting σ* anti-bonding states, and Figure 6c*(v)* shows states of slightly different appearance which can nevertheless be labelled as σ* due to their in-plane character (*cf.* Figure 6c*(iv)*). These π* and σ* states in the B supercell from Figures 6c*(iii)*, *(iv)* and *(v)* are all highly-localised around the C nuclei and *not* the B dopant nucleus, in a complete inversion of the behaviour observed for the N-doped case. This means that the probability of a B 1*s* core electron being promoted to a state localised on the B nucleus is comparatively low in these energy ranges, resulting in the suppression of the π* and σ* regions of the B *K* edge compared to the N case. This inversion in the behaviour of the electron density distribution when compared to the N nucleus, which is more electronegative than its neighbours (due to the excess proton), alludes to the lesser electronegativity of the B nucleus (due to its missing proton) relative to its C counterparts. It can be seen that EELS-active states localised on the B nucleus do exist as revealed by the clear peak in the B *p* DOS indicated in Figure 6c*(vi)*, but that a substantially higher-energy transition of 26 eV above the Fermi energy is required to probe these states. Due to the in-plane character of these states, the corresponding B EELS peak is labelled as the σ* peak.

Thus, in summary, the lesser positive charge of the B nucleus in comparison to its C neighbours has the effect of extending the B EEL spectrum over a broad energy range, culminating in the σ* peak at high energy, the spectroscopic signature of a p-type acceptor.

Conclusions

In summary, the fine structure of electron energy loss the N *K* edge, and for the first time, the B *K* edge were successfully recorded from single N and B fully-substitutional atoms introduced into free-standing single-layer graphene by low-energy ion implantation. The experimental results clearly show the presence of strong peaks at 401 eV and 409 eV in the N *K* ELNES. Theoretical calculations confirm these peaks correspond to π* anti-bonding states and σ* anti-bonding states, respectively, lying at relatively low energies of 1 eV and 8 eV above the Fermi energy. In contrast the experimentally-obtained B *K* ELNES shows a broad and unusual asymmetric shape over the 195 eV to 215 eV range, along with suppressed features at the 189 eV edge onset. Theoretical calculations reveal that this is the result of the energetic unfavourability of π* and σ* states localised on the B dopant at low-to-intermediate energies. Instead, a high-energy transition at 26 eV above the Fermi is required to probe anti-bonding σ* states. A small signal resulting from populating the p-type hole was also predicted and observed experimentally as a weak shoulder at the immediate onset of the B *K* edge. This careful direct comparison of simulations carried out using density functional theory with experimentally-observed edge fine structure suggests the recorded EEL spectra exhibit the direct fingerprints of changes in the local bonding environment (and the corresponding anti-bonding environment) characteristic of p-type and n-type dopant impurities. These results thus provide direct experimental confirmation of p-doping and n-doping in suspended single-layer graphene, and of the effectiveness of ion implantation as a controlled means of achieving this doping, thus paving the way to practical implementations of intrinsic graphene-based FETs.

Methods

Specimen Synthesis

Nitrogen and boron doping of free standing graphene was performed by low energy ion implantation at the Göttingen mass selected ion beam deposition system. The ion implantation was carried out directly on single layer free standing CVD graphene specimens, suspended on Quantifoil TEM grids. A detailed account of the synthesis conditions can be found in Refs.[28,29]

Scanning Transmission electron microscopy

High Angle Annular Dark Field imaging and atomically-resolved electron energy loss spectroscopy were performed in a Nion UltraSTEM100 aberration-corrected dedicated STEM instrument operated at 60 kV, equipped with a Gatan Enfina Spectrometer. The beam convergence was 30 mrad, with a beam current of 60 pA at the sample. In these operating conditions the estimated probe size (full-width at half-maximum – FWHM) is 1.2 Å. The semi-angular ranges of the high-angle annular-dark-field detector and medium-angle annular-dark-field detector were 86-190 and 40-86 mrad, respectively. In these conditions, the HAADF intensity recorded with the probe positioned on an atomic site is approximately proportional to the average atomic number Z of this site as Z^n (n~1.7).[39] HAADF images were processed using a double-Gaussian-filtering routine implemented in Digital Micrograph[55] according to the guidelines described by Krivanek *et al.*[56] The native energy spread of the electron emitter was 0.3 eV and EEL spectra were recorded at a dispersion of 0.2 eV/channel, leading to an effective energy resolution of 0.6 eV (as measured by the full-width at half-maximum of the zero-loss peak in vacuum). The collection angle for the EELS measurements was calibrated at 33 mrad. The EEL spectrum images were acquired using a

0.07 s/pixel dwell time and full (x100) vertical binning of the spectrometer CCD. The N *K,* B *K* and C *K* edge spectra were obtained by integrating the signal over an area of 10x12 pixels of the spectrum images, centred on the corresponding atom, the size of the averaging region corresponding approximately to the atomic radius of these species. The cumulative B *K* spectrum was acquired by defining a 5 Å × 5 Å window around the substitutional atom of interest. The EEL spectrum was acquired by accumulating 0.4 s exposures while scanning repeatedly the subscan window over a 500 s total acquisition time.

Density Functional Theory Calculations

The plane-wave density functional theory (DFT) code CASTEP was used to predict the theoretical core-loss EEL spectra for the substitutional configurations of the N and B dopants and surrounding C atoms. Firstly, the graphene lattice parameter $a = 2.459$ Å was evaluated by relaxing the unit cell using the TS-corrected[57] PBE[58] exchange correlation functional with a plane-wave energy cut off of 550 eV and *k*-point spacings not exceeding 0.035 $Å^{-1}$ as described in Hardcastle *et al.*[59] 4×4 supercells were then constructed with the two substitutional dopant configurations of interest, and these systems were fully relaxed to within a forces tolerance of 0.01 $eVÅ^{-1}$ using BFGS[60–63] minimisation with P1 symmetry and vacuum spacings in the z direction of 20 Å. Initial out-of-plane displacements of 0.01 Å on each dopant were used in these relaxations, and it was found in all cases that the dopants settled into the graphene plane, in contrast to previous instances reported by a number of groups of a Si dopant buckling out of the graphene plane.[33,35] These two fully-relaxed structures were then prepared as the input files for the EELS stages of the calculations. Each atom-specific core-loss spectrum was then obtained by determining the 1*s* core and calculating the matrix elements for transitions to higher-energy unoccupied pseudo-wavefunction states, where the effects of the external perturbation were treated to the level of

the dipole approximation. This was achieved by use of the CASTEP implementation[64] of Blöchl's projector-augmented wave[65] (PAW) formalism as developed by Pickard *et al.*[66] and Rez *et al.*[67] for plane-wave pseudopotentials. The effect of including a core hole in the calculation was deemed to be unrepresentative of the real system (Hardcastle et al. in preparation), consistent with previous works.[33,68] Ground state EELS calculations were performed with an energy cut-off of 800 eV and *k* point spacings no greater than 0.020 $Å^{-1}$on a 6×6×1 Monkhorst-Pack grid[69] as used in Ref. [33] The pseudopotential approach to core-level spectroscopy works by virtue of the fact that the pseudo-wavefunctions can be subjected to a simple linear transformation to recover the all-electron wavefunctions, thereby allowing for direct substitution of the transformed final states into the transition matrix, as explained by Gao *et al.*[64] Instrumental energy broadening effects were accounted for by applying energy-independent FWHM Gaussian broadening of 0.3 eV to the raw calculated spectra. For the energy broadening originating from the finite lifetime of the final state, Lorentzian functions were used for the convolution with FWHM of 0.16 eV, 0.17 eV and 0.18 eV, taken from published values,[70] for B, C and N, respectively. The excited state lifetime broadening was accounted for by using a Lorentzian whose FWHM was linearly dependent on the energy, according to the convention of Fuggle and Inglesfield.[71]

Acknowledgements

SuperSTEM is the U.K. National Facility for Aberration-Corrected STEM, supported by the Engineering and Physical Sciences Research Council (EPSRC). T.P.H. would like to thank the EPSRC for the Doctoral Prize Fellowship which funded this research in part. Computational work was undertaken using the advanced research computing (ARC1 and

ARC2) HPC facilities at The University of Leeds, which provided access to Accelrys Materials Studio.

Supporting Information Available: Unprocessed HAADF STEM images corresponding to Figure1a,b. Raw C *K* edge EELS spectra from neighbouring C in atoms of N dopant – corresponding to Figure 1b in the main text. Band structure calculations of N and B graphene. This material is available free of charge via the Internet at http://pubs.acs.org.

References

(1) Geim, A. K.; Novoselov, K. S. The Rise of Graphene. *Nat Mater* **2007**, *6*, 183–191.

(2) Novoselov, K. S.; Fal′ko, V. I.; Colombo, L.; Gellert, P. R.; Schwab, M. G.; Kim, K. A Roadmap for Graphene. *Nature* **2012**, *490*, 192–200.

(3) Emtsev, K. V; Bostwick, A.; Horn, K.; Jobst, J.; Kellogg, G. L.; Ley, L.; McChesney, J. L.; Ohta, T.; Reshanov, S. A.; Roehrl, J.; *et al.* Towards Wafer-Size Graphene Layers by Atmospheric Pressure Graphitization of Silicon Carbide. *Nat Mater* **2009**, *8*, 203–207.

(4) Hernandez, Y.; Nicolosi, V.; Lotya, M.; Blighe, F. M.; Sun, Z.; De, S.; McGovern, I. T.; Holland, B.; Byrne, M.; Gun'Ko, Y. K.; *et al.* High-Yield Production of Graphene by Liquid-Phase Exfoliation of Graphite. *Nat Nanotechnol* **2008**, *3*, 563–568.

(5) Zhang, Y. B.; Tan, Y. W.; Stormer, H. L.; Kim, P. Experimental Observation of the Quantum Hall Effect and Berry's Phase in Graphene. *Nature* **2005**, *438*, 201–204.

(6) Castro Neto, A. H.; Guinea, F.; Peres, N. M. R.; Novoselov, K. S.; Geim, A. K. The Electronic Properties of Graphene. *Rev Mod Phys* **2009**, *81*, 109–162.

(7) Berger, C.; Song, Z.; Li, X.; Wu, X.; Brown, N.; Naud, C.; Mayou, D.; Li, T.; Hass, J.; Marchenkov, A. N.; *et al.* Electronic Confinement and Coherence in Patterned Epitaxial Graphene. *Science* **2006**, *312*, 1191–1196.

(8) Roy-Mayhew, J. D.; Bozym, D. J.; Punckt, C.; Aksay, I. A. Functionalized Graphene as a Catalytic Counter Electrode in Dye-Sensitized Solar Cells. *ACS Nano* **2010**, *4*, 6203–6211.

(9) Wang, S.; Ang, P. K.; Wang, Z.; Tang, A. L. L.; Thong, J. T. L.; Loh, K. P. High Mobility, Printable, and Solution-Processed Graphene Electronics. *Nano Lett* **2010**, *10*, 92–98.

(10) Bolotin, K. I.; Sikes, K. J.; Jiang, Z.; Klima, M.; Fudenberg, G.; Hone, J.; Kim, P.; Stormer, H. L. Ultrahigh Electron Mobility in Suspended Graphene. *Solid State Commun* **2008**, *146*, 351–355.

(11) Kim, K.; Choi, J.-Y.; Kim, T.; Cho, S.-H.; Chung, H.-J. A Role for Graphene in Silicon-Based Semiconductor Devices. *Nature* **2011**, *479*, 338–344.

(12) Schwierz, F. Graphene Transistors. *Nat Nanotechnol* **2010**, *5*, 487–496.

(13) Li, X.; Wang, X.; Zhang, L.; Lee, S.; Dai, H. Chemically Derived, Ultrasmooth Graphene Nanoribbon Semiconductors. *Science* **2008**, *319*, 1229–1232.

(14) Han, M. Y.; Özyilmaz, B.; Zhang, Y.; Kim, P. Energy Band-Gap Engineering of Graphene Nanoribbons. *Phys Rev Lett* **2007**, *98*, 206805.

(15) Terrones, H.; Lv, R.; Terrones, M.; Dresselhaus, M. S. The Role of Defects and Doping in 2D Graphene Sheets and 1D Nanoribbons. *Reports Prog Phys* **2012**, *75*, 62501.

(16) Wehling, T. O.; Katsnelson, M. I.; Lichtenstein, A. I. Impurities on Graphene: Midgap States and Migration Barriers. *Phys Rev B* **2009**, *80*, 85428.

(17) Wang, H.; Maiyalagan, T.; Wang, X. Review on Recent Progress in Nitrogen-Doped Graphene: Synthesis, Characterization, and Its Potential Applications. *ACS Catal* **2012**, *2*, 781–794.

(18) Cruz-Silva, E.; López-Urías, F.; Muñoz-Sandoval, E.; Sumpter, B. G.; Terrones, H.; Charlier, J.-C.; Meunier, V.; Terrones, M. Electronic Transport and Mechanical Properties of Phosphorus and Phosphorus Nitrogen-Doped Carbon Nanotubes. *ACS Nano* **2009**, *3*, 1913–1921.

(19) Panchakarla, L. S.; Subrahmanyam, K. S.; Saha, S. K.; Govindaraj, A.; Krishnamurthy, H. R.; Waghmare, U. V; Rao, C. N. R. Synthesis, Structure, and Properties of Boron- and Nitrogen-Doped Graphene. *Adv Mater* **2009**, *21*, 4726–4730.

(20) Wang, L.; Sofer, Z.; Šimek, P.; Tomandl, I.; Pumera, M. Boron-Doped Graphene: Scalable and Tunable P-Type Carrier Concentration Doping. *J Phys Chem C* **2013**, *117*, 23251–23257.

(21) Casolo, S.; Martinazzo, R.; Tantardini, G. F. Band Engineering in Graphene with Superlattices of Substitutional Defects. *J Phys Chem* **2010**, *115*, 3250–3256.

(22) Zhou, Y.-C.; Zhang, H.-L.; Deng, W.-Q. A 3N Rule for the Electronic Properties of Doped Graphene. *Nanotechnology* **2013**, *24*, 225705.

(23) Schiros, T.; Nordlund, D.; Pálová, L.; Prezzi, D.; Zhao, L.; Kim, K. S.; Wurstbauer, U.; Gutiérrez, C.; Delongchamp, D.; Jaye, C.; *et al.* Connecting Dopant Bond Type with Electronic Structure in N-Doped Graphene. *Nano Lett* **2012**, *12*, 4025–4031.

(24) Tison, Y.; Lagoute, J.; Repain, V.; Chacon, C.; Girard, Y.; Rousset, S.; Joucken, F.; Sharma, D.; Henrard, L.; Amara, H.; *et al.* Electronic Interaction between Nitrogen Atoms in Doped Graphene. *ACS Nano* **2015**, *9*, 670–678.

(25) Koch, R. J.; Weser, M.; Zhao, W.; Viñes, F.; Gotterbarm, K.; Kozlov, S. M.; Höfert, O.; Ostler, M.; Papp, C.; Gebhardt, J.; *et al.* Growth and Electronic Structure of Nitrogen-Doped Graphene on Ni(111). *Phys Rev B* **2012**, *86*, 75401.

(26) Gebhardt, J.; Koch, R. J.; Zhao, W.; Höfert, O.; Gotterbarm, K.; Mammadov, S.; Papp, C.; Görling, A.; Steinrück, H.-P.; Seyller, T. Growth and Electronic Structure of Boron-Doped Graphene. *Phys Rev B* **2013**, *87*, 155437.

(27) Usachov, D.; Vilkov, O.; Grüneis, A.; Haberer, D.; Fedorov, A.; Adamchuk, V. K.; Preobrajenski, A. B.; Dudin, P.; Barinov, A.; Oehzelt, M.; *et al.* Nitrogen-Doped Graphene: Efficient Growth, Structure, and Electronic Properties. *Nano Lett* **2011**, *11*, 5401–5407.

(28) Xu, Y.; Zhang, K.; Brüsewitz, C.; Wu, X.; Hofsäss, H. C. Investigation of the Effect of Low Energy Ion Beam Irradiation on Mono-Layer Graphene. *AIP Adv* **2013**, *3*, 072120.

(29) Bangert, U.; Pierce, W.; Kepaptsoglou, D. M.; Ramasse, Q.; Zan, R.; Gass, M. H.; Van den Berg, J. a; Boothroyd, C. B.; Amani, J.; Hofsäss, H. Ion Implantation of Graphene-Toward IC Compatible Technologies. *Nano Lett* **2013**, *13*, 4902–4907.

(30) Willke, P.; Amani, J. A.; Sinterhauf, A.; Thakur, S.; Kotzott, T.; Druga, T.; Weikert, S.; Maiti, K.; Hofsäss, H.; Wenderoth, M. Doping of Graphene by Low-Energy Ion Beam Implantation: Structural, Electronic, and Transport Properties. *Nano Lett* **2015**.

(31) Ahlgren, E. H.; Kotakoski, J.; Krasheninnikov, A. V. Atomistic Simulations of the Implantation of Low-Energy Boron and Nitrogen Ions into Graphene. *Phys Rev B* **2011**, *83*, 115424.

(32) Lovejoy, T. C.; Ramasse, Q. M.; Falke, M.; Kaeppel, A.; Terborg, R.; Zan, R.; Dellby, N.; Krivanek, O. L. Single Atom Identification by Energy Dispersive X-Ray Spectroscopy. *Appl Phys Lett* **2012**, *100*, 154101.

(33) Ramasse, Q. M.; Seabourne, C. R.; Kepaptsoglou, D.-M.; Zan, R.; Bangert, U.; Scott, A. J. Probing the Bonding and Electronic Structure of Single Atom Dopants in Graphene with Electron Energy Loss Spectroscopy. *Nano Lett* **2013**, *13*, 4989–4995.

(34) Hansen, L. P.; Ramasse, Q. M.; Kisielowski, C.; Brorson, M.; Johnson, E.; Topsøe, H.; Helveg, S. Atomic-Scale Edge Structures on Industrial-Style MoS2 Nanocatalysts. *Angew Chemie Int Ed* **2011**, *50*, 10153–10156.

(35) Zhou, W.; Kapetanakis, M. D.; Prange, M. P.; Pantelides, S. T.; Pennycook, S. J.; Idrobo, J.-C. Direct Determination of the Chemical Bonding of Individual Impurities in Graphene. *Phys Rev Lett* **2012**, *109*, 206803.

(36) Nicholls, R. J.; Murdock, A. T.; Tsang, J.; Britton, J.; Pennycook, T. J.; Koós, A.; Nellist, P. D.; Grobert, N.; Yates, J. R. Probing the Bonding in Nitrogen-Doped Graphene Using Electron Energy Loss Spectroscopy. *ACS Nano* **2013**, *7*, 7145–7150.

(37) Warner, J. H.; Liu, Z.; He, K.; Robertson, A. W.; Suenaga, K. Sensitivity of Graphene Edge States to Surface Adatom Interactions. *Nano Lett* **2013**, *13*, 4820–4826.

(38) Arenal, R.; March, K.; Ewels, C. P.; Rocquefelte, X.; Kociak, M.; Loiseau, A.; Stéphan, O. Atomic Configuration of Nitrogen-Doped Single-Walled Carbon Nanotubes. *Nano Lett* **2014**, *14*, 5509–5516.

(39) Krivanek, O. L.; Chisholm, M. F.; Nicolosi, V.; Pennycook, T. J.; Corbin, G. J.; Dellby, N.; Murfitt, M. F.; Own, C. S.; Szilagyi, Z. S.; Oxley, M. P.; *et al.* Atom-by-Atom Structural and Chemical Analysis by Annular Dark-Field Electron Microscopy. *Nature* **2010**, *464*, 571–574.

(40) Zhao, L.; He, R.; Rim, K. T.; Schiros, T.; Kim, K. S.; Zhou, H.; Gutiérrez, C.; Chockalingam, S. P.; Arguello, C. J.; Pálová, L.; *et al.* Visualizing Individual Nitrogen Dopants in Monolayer Graphene. *Science* **2011**, *333*, 999–1003.

(41) Bhattacharyya, S. Investigation on the Change in Structure of Tetrahedral Amorphous Carbon by a Large Amount of Nitrogen Incorporation. *Diam Relat Mater* **2000**, *9*, 544–547.

(42) Nesting, D. C.; Badding, J. V. High-Pressure Synthesis of sp2-Bonded Carbon Nitrides. *Chem Mater* **1996**, *8*, 1535–1539.

(43) Warner, J. H.; Lin, Y.-C.; He, K.; Koshino, M.; Suenaga, K. Stability and Spectroscopy of Single Nitrogen Dopants in Graphene at Elevated Temperatures. *ACS Nano* **2014**, *8*, 11806–11815.

(44) Seabourne, C. R.; Brydson, R.; Brown, A. P.; Latham, C. D.; Heggie, M. I.; Scott, A. J. EELS Modelling of Graphitisation. *J Phys Conf Ser* **2014**, *522*, 12014.

(45) Arenal, R.; Kociak, M.; Zaluzec, N. J. High-Angular-Resolution Electron Energy Loss Spectroscopy of Hexagonal Boron Nitride. *Appl Phys Lett* **2007**, *90*, 204105.

(46) Susi, T.; Kotakoski, J.; Kepaptsoglou, D.; Mangler, C.; Lovejoy, T. C.; Krivanek, O. L.; Zan, R.; Bangert, U.; Ayala, P.; Meyer, J. C.; *et al.* Silicon–Carbon Bond Inversions Driven by 60-keV Electrons in Graphene. *Phys Rev Lett* **2014**, *113*, 115501.

(47) Susi, T.; Kotakoski, J.; Arenal, R.; Kurasch, S.; Jiang, H.; Skakalova, V.; Stephan, O.; Krasheninnikov, A. V; Kauppinen, E. I.; Kaiser, U.; *et al.* Atomistic Description of Electron Beam Damage in Nitrogen-Doped Graphene and Single-Walled Carbon Nanotubes. *ACS Nano* **2012**, *6*, 8837–8846.

(48) Norimatsu, W.; Hirata, K.; Yamamoto, Y.; Arai, S.; Kusunoki, M. Epitaxial Growth of Boron-Doped Graphene by Thermal Decomposition of B 4 C. *J Phys Condens Matter* **2012**, *24*, 314207.

(49) Serin, V.; Brydson, R.; Scott, A.; Kihn, Y.; Abidate, O.; Maquin, B.; Derré, A. Evidence for the Solubility of Boron in Graphite by Electron Energy Loss Spectroscopy. *Carbon N Y* **2000**, *38*, 547–554.

(50) Alem, N.; Ramasse, Q. M.; Seabourne, C. R.; Yazyev, O. V; Erickson, K.; Sarahan, M. C.; Kisielowski, C.; Scott, A. J.; Louie, S. G.; Zettl, A. Subangstrom Edge Relaxations Probed by Electron Microscopy in Hexagonal Boron Nitride. *Phys Rev Lett* **2012**, *109*, 205502.

(51) Suenaga, K.; Kobayashi, H.; Koshino, M. Core-Level Spectroscopy of Point Defects in Single Layer H-BN. *Phys Rev Lett* **2012**, *108*, 75501.

(52) Salpeter, E. E.; Bethe, H. A. A Relativistic Equation for Bound-State Problems. *Phys Rev* **1951**, *84*, 1232–1242.

(53) Morris, A. J.; Nicholls, R. J.; Pickard, C. J.; Yates, J. R. OptaDOS: A Tool for Obtaining Density of States, Core-Level and Optical Spectra from Electronic Structure Codes. *Comput Phys Commun* **2014**, *185*, 1477–1485.

(54) Yates, J. R.; Wang, X.; Vanderbilt, D.; Souza, I. Spectral and Fermi Surface Properties from Wannier Interpolation. *Phys Rev B* **2007**, *75*, 195121.

(55) Pierce, W. R. High-Resolution Transmission Electron Microscopy and Electron Energy Loss Spectroscopy of Doped Nanocarbons, The University of Manchester, 2014.

(56) Krivanek, O. L.; Dellby, N.; Murfitt, M. F.; Chisholm, M. F.; Pennycook, T. J.; Suenaga, K.; Nicolosi, V. Gentle STEM: ADF Imaging and EELS at Low Primary Energies. *Ultramicroscopy* **2010**, *110*, 935–945.

(57) Tkatchenko, A.; Scheffler, M. Accurate Molecular Van Der Waals Interactions from Ground-State Electron Density and Free-Atom Reference Data. *Phys Rev Lett* **2009**, *102*, 73005.

(58) Perdew, J. P.; Burke, K.; Ernzerhof, M. Generalized Gradient Approximation Made Simple. *Phys Rev Lett* **1996**, *77*, 3865–3868.

(59) Hardcastle, T. P.; Seabourne, C. R.; Zan, R.; Brydson, R. M. D.; Bangert, U.; Ramasse, Q. M.; Novoselov, K. S.; Scott, A. J. Mobile Metal Adatoms on Single Layer, Bilayer, and Trilayer Graphene: An Ab Initio DFT Study with van Der Waals Corrections Correlated with Electron Microscopy Data. *Phys Rev B* **2013**, *87*, 195430.

(60) Broyden, C. G. The Convergence of a Class of Double-Rank Minimization Algorithms 1. General Considerations. *IMA J Appl Math* **1970**, *6*, 76–90.

(61) Broyden, C. G. The Convergence of a Class of Double-Rank Minimization Algorithms: 2. The New Algorithm. *IMA J Appl Math* **1970**, *6*, 222–231.

(62) Fletcher, R. A New Approach to Variable Metric Algorithms. *Comput J* **1970**, *13* , 317–322.

(63) Goldfarb, D. A Family of Variable-Metric Methods Derived by Variational Means. *Math Comput* **1970**, *24*, 23–23.

(64) Gao, S.-P.; Pickard, C. J.; Perlov, A.; Milman, V. Core-Level Spectroscopy Calculation and the Plane Wave Pseudopotential Method. *J Phys Condens Matter* **2009**, *21*, 104203.

(65) Blöchl, P. E. Projector Augmented-Wave Method. *Phys Rev B* **1994**, *50*, 17953–17979.

(66) Pickard, C. J.; Payne, M. Ab Initio EELS: Beyond the Fingerprint. In *Electron Microscopy and Analysis 1997*; Rodenburg JM, Ed.; IOP Publishing LTD, 1997; p. 175.

(67) Rez, P.; Alvarez, J. R.; Pickard, C. Calculation of near Edge Structure. *Ultramicroscopy* **1999**, *78*, 175–183.

(68) Rez, P. Perfection in Theoretical Modeling of Electron Energy Loss Spectra: Is It Attainable? *Microsc Microanal* **2006**, *12*, 108–109.

(69) Monkhorst, H. J.; Pack, J. D. Special Points for Brillouin-Zone Integrations. *Phys Rev B* **1976**, *13*, 5188–5192.

(70) Krause, M. O. Atomic Radiative and Radiationless Yields for K and L Shells. *J Phys Chem Ref Data* **1979**, *8*, 307.

(71) Fuggle, J. C.; Inglesfield, J. E. Introduction. In *Unoccupied Electronic States SE - 1*; Fuggle, J.; Inglesfield, J., Eds.; Topics in Applied Physics; Springer Berlin Heidelberg, 1992; Vol. 69, pp. 1–23.

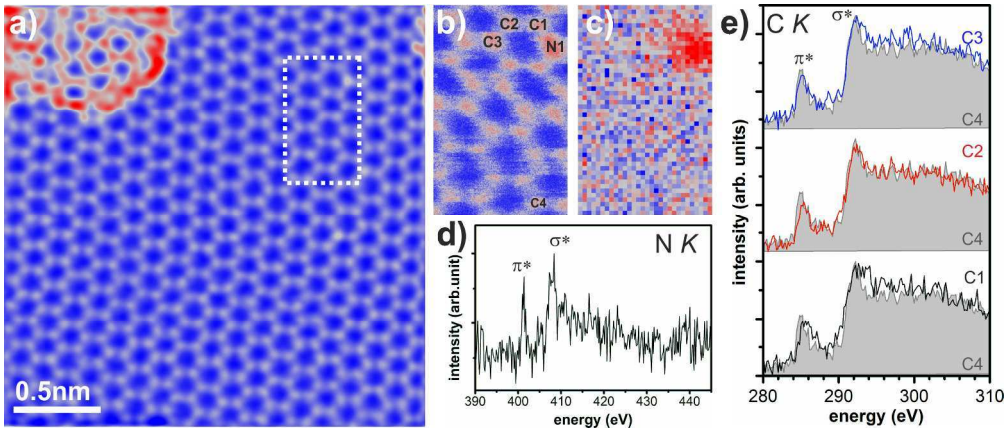

Figure 1. a) HAADF STEM image of N-implanted graphene sample (filtered using the approach of Krivanek et al.[39] – unprocessed data available in supplementary material), b) HAADF signal acquired simultaneously with the EELS spectrum image acquired in the region defined by the dashed rectangle in (a), c) map of the N *K* EELS signal shown in (d), e) normalised C *K* edge EELS spectra from neighbouring C atoms as labelled in (b), showing changes in their near-edge fine structure.
237x100mm (300 x 300 DPI)

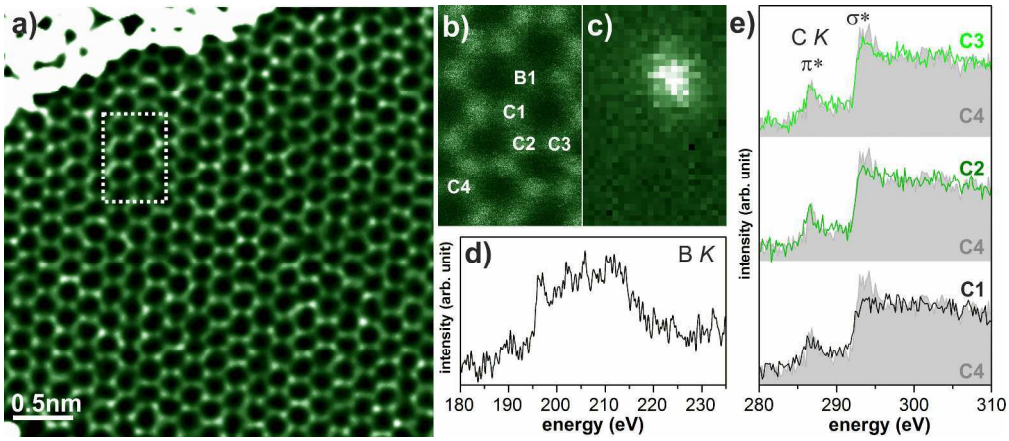

Figure 2. a) HAADF-STEM image of a B-implanted graphene sample, processed with a double Gaussian filter to remove probe tail effects[39]; b) HAADF signal acquired simultaneously with the EELS spectrum image, c) map of the B *K* EELS signal shown in (d), e) C *K* edge EELS spectra from single neighbouring C atoms, showing changes in their near edge fine structure.
287x124mm (300 x 300 DPI)

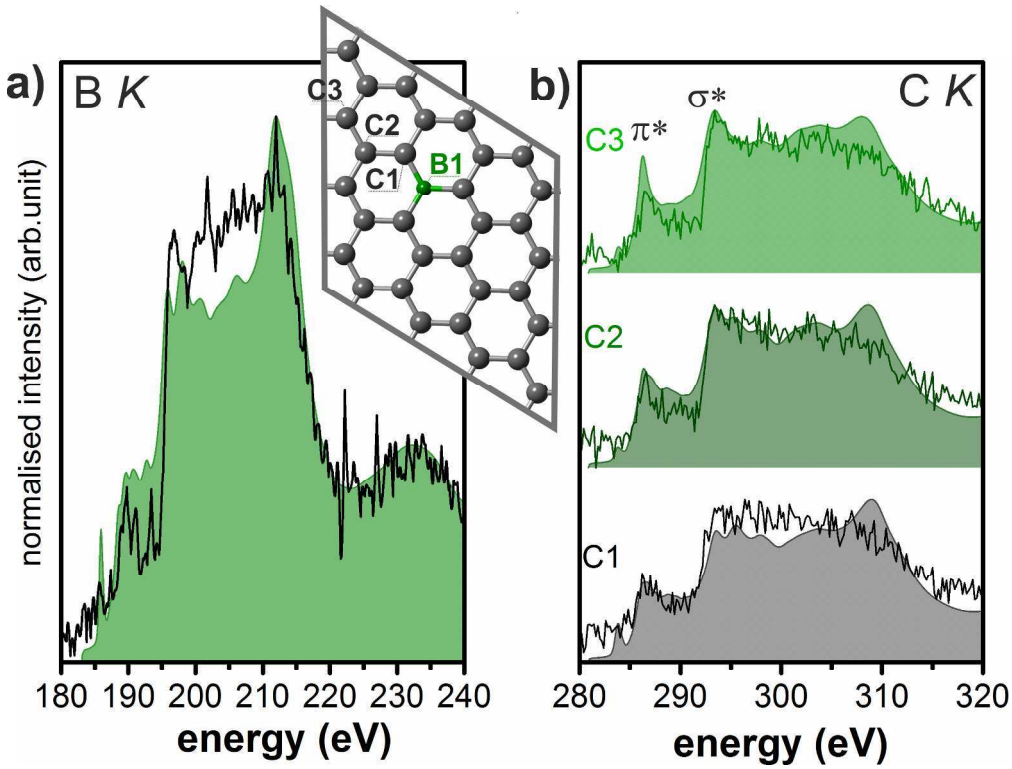

Figure 4. a) B *K* and b) C *K* background subtracted experimental spectra (solid lines), plotted against spectra calculated by DFT (shaded areas). The theoretical spectra were rigidly translated to the experimental spectra for reading clarity; no stretching of the energy axis was applied. The nuclear positions and electron density were fully relaxed by DFT calculations using the model inset in (a).
249x189mm (300 x 300 DPI)

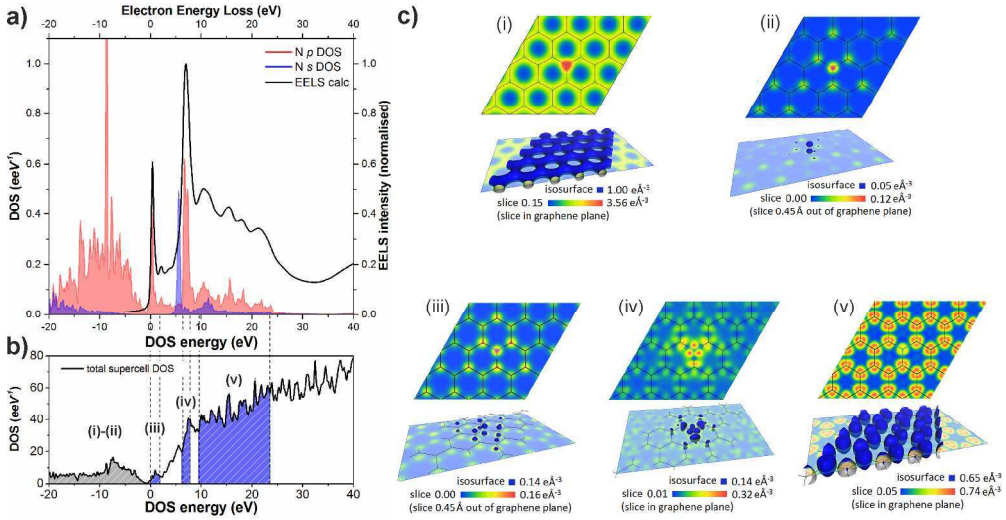

Figure 5. Calculated electronic states for single substitutional N dopants in graphene. a) overlaid *p* DOS, *p* DOS and calculated N *K* EELS spectrum; b) total DOS: all states lying within a chosen energy window are highlighted in the shaded areas. The states that lie within that energy window are populated and the density is plotted and displayed as 2D slices from above the lattice: c)(i)-(ii) excess density on the N dopant and density slice showing the single state constituting the negative charge carrier which has the appearance of a p_z-like orbital and is occupied in the ground state; (iii)-(v) unoccupied states attributable to EELS peaks of interest in (a). Specifically: (iii) π*-like states, (iv) σ*-like states both highly localised on the dopant and (v) high-energy states localised on the C nuclei
231x119mm (300 x 300 DPI)

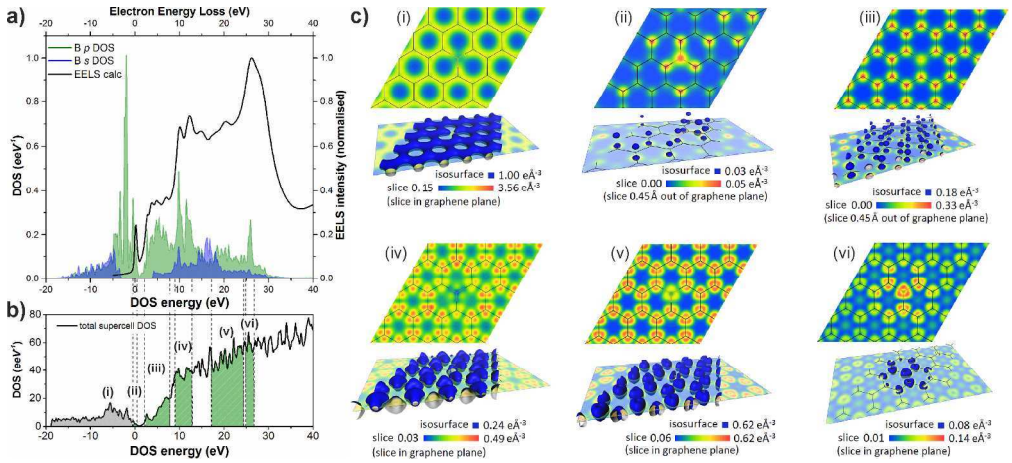

Figure 6. Calculated electronic states for single substitutional B dopants in graphene. a) overlaid *p* DOS, *s* DOS and calculated B *K* EELS spectrum. b) total DOS: all states lying within a chosen energy window are highlighted in the shaded areas. The states that lie within that energy window are populated and the density is plotted and displayed as 2D slices from above the lattice in c) (i) ground states, showing the missing charge density on the dopant causing the Fermi energy to sink into the π band, constituting the hole (see also Figure S4b of the supplementary information provided. Panels (ii)-(vi) correspond to unoccupied states attributable to EELS peaks of interest in (a); (ii) the π state occupying the charge carrier hole, (iii) π*-like states and (iv) σ*-like states both mostly localised around the C nuclei with a noticeably lower accumulation of charge around the dopant; (v) high energy σ*-like states localised on the C nuclei and (vi) high energy σ*-like states localised on the dopant.
262x118mm (300 x 300 DPI)

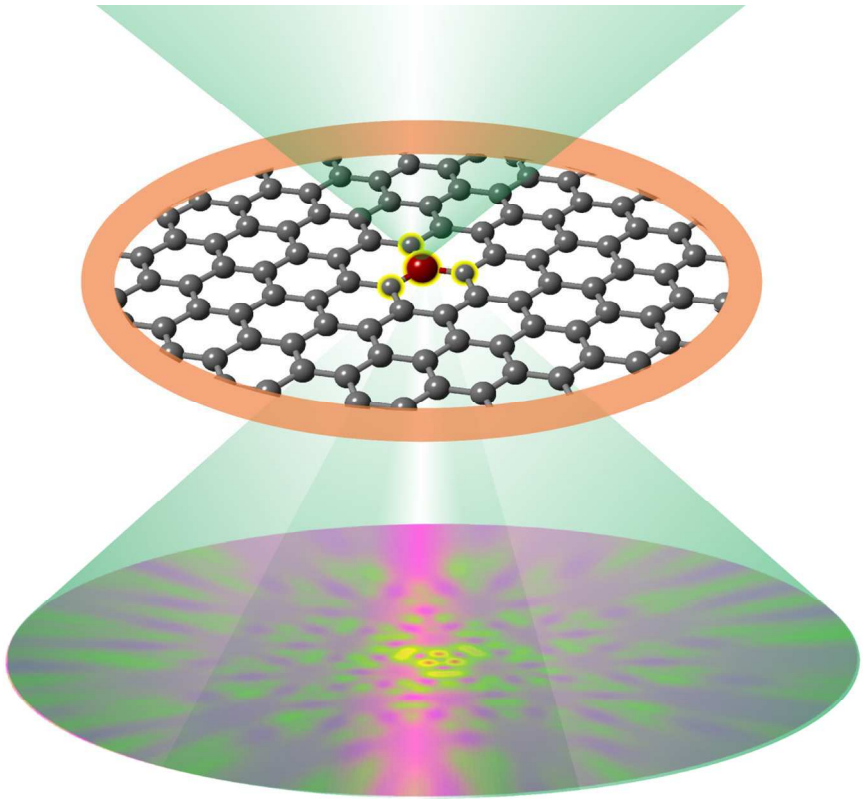

120x95mm (299 x 299 DPI)